Journal of Materials Chemistry A

Accepted Manuscript

This article can be cited before page numbers have been issued, to do this please use: F. Wang, A. Chemseddine, F. Abdi, R. van de Krol and S. Berglund, *J. Mater. Chem. A*, 2017, DOI: 10.1039/C7TA03009F.

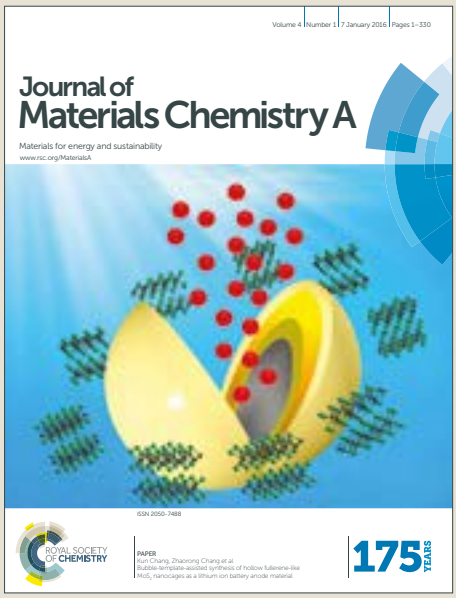

ROYAL SOCIETY OF CHEMISTRY

rsc.li/materials-a

View Article Online
DOI: 10.1039/C7TA03009F

Journal of Materials Chemistry A

ARTICLE

Spray pyrolysis of $CuBi_2O_4$ photocathodes: improved solution chemistry for highly homogeneous thin films

Received 00th March 2017,
Accepted 00th March 2017

DOI: 10.1039/x0xx00000x

www.rsc.org/

Fuxian Wang, Abdelkrim Chemseddine, Fatwa F. Abdi, Roel van de Krol, Sean P. Berglund*

Dense, homogeneous $CuBi_2O_4$ thin films are prepared, for the first time, by spray pyrolysis. Major challenges related to the chemical stability of the precursor solution and spreading behavior of the sprayed droplets are revealed and addressed. Triethyl orthoformate (TEOF) is added as a water scavenger to avoid fast hydrolysis and polycondensation of bismuth ions in the precursor solution, thereby reducing powder formation during the spray deposition process. Polyethylene glycol (PEG) is used to improve the spreading behavior of sprayed droplets over the entire $CuBi_2O_4$ film surface, which prevents powder formation completely and allows for the deposition of dense, homogeneous films with thicknesses over 420 nm. These highly uniform $CuBi_2O_4$ thin films are well-suited for fundamental studies on the optical and photoelectrochemical properties. Additionally, they produce record photocurrent densities for $CuBi_2O_4$ up to 2.0 mA/cm^2 under AM 1.5 simulated sunlight along with incident photon-to-current efficiency (IPCE) and absorbed photon-to-current efficiency (APCE) values up to 14 % and 23 %, respectively (for 550 nm light at 0.6 V_{RHE} with H_2O_2 as an electron scavenger).

Introduction

$CuBi_2O_4$, a p-type metal oxide semiconductor, has recently attracted attention as a photocathode material for water splitting due to its suitable bandgap of 1.5 - 1.8 eV and its exceptionally positive photocurrent onset potential near +1 V vs. RHE.[1, 2] Under AM 1.5 illumination the maximal theoretical photocurrent density is 19.7 – 29.0 mA/cm^2, assuming all photons with energies higher than the bandgap are absorbed and utilized with 100 % efficiency.[3] However, the experimental photocurrent densities reported so far have been well below this theoretical limit.[1, 2, 4, 5] Possible reasons include relatively poor charge carrier transport within the bulk material, which is a common challenge for metal oxide photoelectrodes, surface defects or states resulting in excessive recombination of photo-generated carriers at the surface, and sluggish reaction kinetics for the proton reduction reaction.[6] Attempts have been made to pinpoint the main performance limiting factors, but in-depth analysis has been made difficult since all the reported $CuBi_2O_4$ films showed a highly porous and irregular structure[2, 5, 7] and/or incomplete substrate coverage.[4] Such irregular structures usually result in a high amount of optical scattering, which presents additional challenges and complications for the implementation of multiple photoelectrodes in a tandem cell configuration.[8] Therefore, new deposition techniques that produce dense, homogeneous $CuBi_2O_4$ thin films are needed to unravel the basic material properties so that the performance limiting factors can be thoroughly quantified. Each problem can then be systematically addressed to improve the photocurrent density towards the theoretical limit, as was successfully done for other metal oxide photoelectrodes like $BiVO_4$[9-11] and Cu_2O[12, 13].

In this work we report, for the first time, the synthesis of high quality, dense, and homogeneous $CuBi_2O_4$ thin film photocathodes by spray pyrolysis. To accomplish this, precursor solutions containing Cu^{2+} and Bi^{3+} ions were mixed with various additives to prevent undesired side reactions and insufficient film adherence during the spray pyrolysis process. The chemical composition and stability of the precursor solutions were analyzed in detail using infrared spectroscopy and the resulting $CuBi_2O_4$ thin films were characterized using optical and photoelectrochemical measurements. The dense, homogenous $CuBi_2O_4$ thin film photocathodes synthesized using the optimized spray pyrolysis recipe set a new benchmark AM1.5 photocurrent density for $CuBi_2O_4$ of 2.0 mA/cm^2 at 0.6 V_{RHE} with H_2O_2 as an electron scavenger.

Results and discussion

Optimization of Spray Pyrolysis Recipe for $CuBi_2O_4$ Photocathodes

In this study, the spray pyrolysis precursor solution was prepared by dissolving $Bi(NO_3)_3 \bullet 5H_2O$ in acetic acid and mixing it with $Cu(NO_3)_2 \bullet 3H_2O$ in ethanol to a $Cu(NO_3)_2 \bullet 3H_2O$: $Bi(NO_3)_3 \bullet 5H_2O$ molar ratio of 1 : 2 in order to match the stoichiometry of $CuBi_2O_4$. The combination of Cu^{2+} and Bi^{3+} ions, H_2O, acetic acid, and ethanol resulted in major challenges related to the stability of the solution and spreading behavior

Helmholtz-Zentrum Berlin für Materialien und Energie GmbH, Institute for Solar Fuels, Hahn-Meitner-Platz 1, 14109 Berlin, Germany. Email: sean.berglund@helmholtz-berlin.de

† Electronic Supplementary Information (ESI) available: SEM images, XRD pattern, photographs of different spray solutions and the precipitate, ATR-IR spectra, Tauc plots, LSV scans for $CuBi_2O_4$ in 0.1 M KOH, current density and power spectra for IPCE measurement. See DOI: 10.1039/x0xx00000x

View Article Online
DOI: 10.1039/C7TA03009F

of droplets during spray pyrolysis. To overcome these challenges small amounts of triethyl orthoformate (TEOF) and polyethylene glycol (PEG) were added. In this section we discuss the chemistry of the precursor solution and the resulting morphology of the $CuBi_2O_4$ thin films prepared under the following conditions: (1) without additives, (2) with TEOF, and (3) with TEOF and PEG.

First we investigate $CuBi_2O_4$ thin films prepared without any additives. $CuBi_2O_4$ precursor solution concentrations of 2, 10, and 20 mM (i.e. 20 mM $Cu(NO_3)_2 \bullet 3H_2O$ and 40 mM $Bi(NO_3)_3 \bullet 5H_2O$) were prepared with an acetic acid : ethanol ratio of 1 : 9. The spray volume was adjusted for each concentration so that a constant mol amount of Cu^{2+} and Bi^{3+} was sprayed. SEM images comparing $CuBi_2O_4$ films produced from these three concentrations are included in Figure S1 in the Supporting Information. The film produced using a 20 mM precursor concentration shows the most homogenous distribution of $CuBi_2O_4$ crystallites on the surface. X-ray diffraction (XRD) was used to confirm that all of the $CuBi_2O_4$ thin films prepared in this study are crystalline (see Figure S2). The X-ray diffractogram for the prepared film (labeled as "without additives") matches very well with the reference pattern for tetragonal $CuBi_2O_4$ (PDF# 00-042-0334, kusachiite, tetragonal crystal structure, space group P4/ncc).

A photograph and cross section SEM images of this $CuBi_2O_4$ film are shown in Figure 1. The thickness of the film is estimated to be ~ 50 nm. Although the $CuBi_2O_4$ thin film deposited in the center of the substrate was fairly homogeneous (Figure 1a), at the edges of the substrate the film surface was covered with large particulate agglomerations on the order of 1-3 μm in diameter (Figure 1b). As shown in the photograph, these agglomerates on the edges of the substrate are rough and opaque in appearance (powder-like). Attempts to synthesize $CuBi_2O_4$ films thicker than 50 nm by spraying more than 28 mL were hampered by powder formation both at the edges and in the center of the substrate accompanied by cracking and flaking of the top layer.

Since the amount of powder on the film surface increased with increasing spray volume, and hence total spray time, it was suspected that the powder formation was caused by chemical changes in the precursor solution over time. When the 20 mM precursor solution was first prepared it was highly transparent, but within 3.5 h it turned opaque and solid precipitates became visible (see Figure S3). XRD measurements on the dried and annealed precipitate (500 °C in air for 2 h) revealed a diffractogram that matches closely to

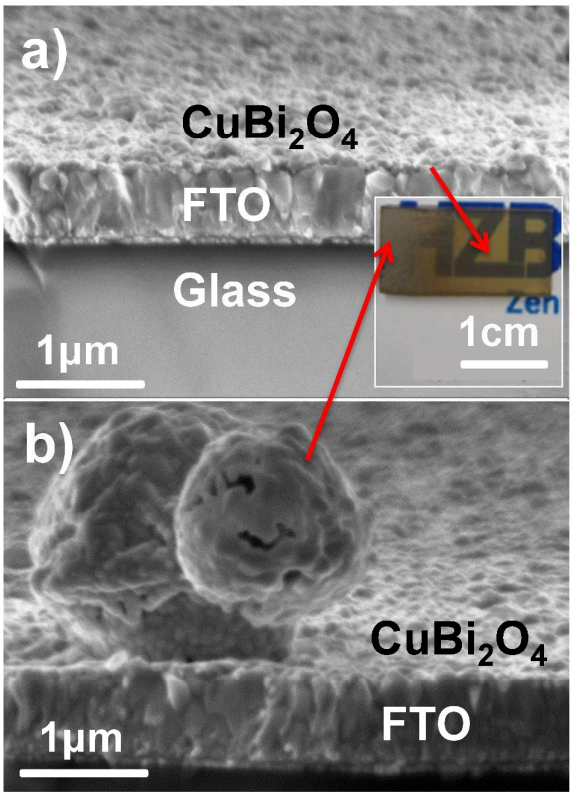

Figure 1. Photograph and cross section SEM images of a ~ 50 nm $CuBi_2O_4$ thin film synthesized on an FTO substrate by spraying 28 mL of 20 mM precursor solution without additives (a) in the center of the substrate and (b) at the edge of the substrate. The substrate temperature was 450 °C.

the reference pattern for Bi_2O_3 (PDF # 01-071-0465), as shown in Figure S4. This result indicates that hydrolysis, polycondensation, and precipitation predominantly affect the bismuth ions while copper ions remain in the supernatant solution. It has been demonstrated that Bi^{3+} ions can be easily hydrolyzed in the presence of water according to the following reaction,[14]

$$Bi_nO_{n-1}^{(n+2)+} + H_2O + Bi^{3+} \rightarrow Bi_{n+1}O_n^{(n+3)+} + 2H^+ \quad (1)$$

Since the precursor solution contains a significant amount of water from $Bi(NO_3)_3 \bullet 5H_2O$ and $Cu(NO_3)_2 \bullet 3H_2O$, the above reaction likely occurs.

View Article Online
DOI: 10.1039/C7TA03009F

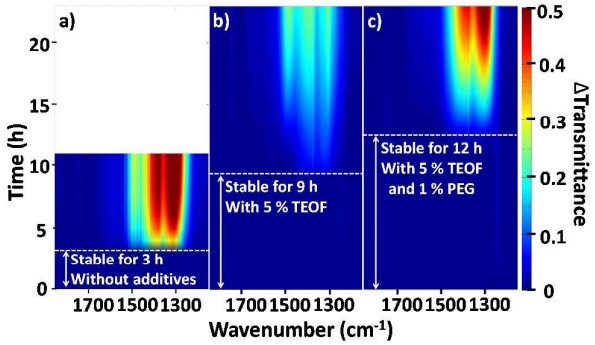

Figure 2. Relative change in transmittance (ΔT) for the 20 mM $CuBi_2O_4$ precursor in 1 : 9 acetic acid : ethanol (a) without additives; (b) with 5 % TEOF; (c) with 5 % TEOF and 1 % PEG. Transmittance was extracted from Figures S7, S8, and S9 and divided by the reference spectrum (measured at 0 h) to obtain the relative changes in the optical transmittance (ΔT) as a function of time and the wavenumber.

To confirm this, a detailed in situ attenuated total reflection infrared (ATR-IR) study was carried out. As reference, the various solvents and additives were measured individually (water, acetic acid, ethanol, TEOF, PEG) as well as the most likely reaction product from the esterification of ethanol and acetic acid (ethyl acetate) and the precipitate formed by hydrolysis of Bi^{3+}. The ATR-IR spectra for these chemicals are included in the Supporting Information (Figures S5 and S6). Since our goal was to observe the chemical changes taking place in the solution, we were especially interested in the vibrational modes of the bismuth-containing precipitate. The precipitate showed a strong IR band at 1301 cm^{-1}. This can be assigned to a nitrate vibration and indicates the presence of bismuth oxynitrate.[15] A decrease in transmittance around 1301 cm^{-1} was therefore used as an indication of precursor instability. Figure 2a shows a color plot of the relative change in transmittance (ΔT) vs. wavenumber and time for the precursor solution without additives. No noticeable change in the transmittance was observed for the first 3 h, but between 3 h and 4 h, there was an abrupt decrease in transmittance at 1301 cm^{-1}, suggesting that bismuth oxynitrate began to settle near the ATR-IR window. This is in agreement with the visual observations of the precursor solution (Figure S3).

Although we did not observe a change in IR transmittance during the first 3 h, it is likely that precipitation begins much sooner than 3 h. During initial precipitation, however, the particle size is likely too small to be detected visually or by ATR-IR.[16] For small particles the intensity of the nitrate vibration of bismuth oxynitrate at 1301 cm^{-1} can be very weak due to the long wavelength and short penetration depth of the IR light into the solution.

Another possible explanation of the observed change in IR transmittance is the esterification reaction of our solvents. Acetic acid and ethanol may react according to the following reaction:

$$CH_3COOH + CH_3CH_2OH \rightarrow CH_3COOCH_2CH_3 + H_2O \quad (2)$$

However, no signal is found for ethyl acetate at 1745 cm^{-1} (C=O) or 1240 cm^{-1} (C-O)[17] (see Figure S5 for IR reference spectra of various solvents). This is further confirmed by a 24 h ATR-IR measurement of solution containing only 1 : 9 acetic acid : ethanol, in which no ethyl acetate signal was observed (Figure S10). This is likely due to very slow kinetics for the esterification reaction (reaction 2) without the presence of a catalyst.[18] Alternatively, the equilibrium of reaction (2) may lie too far to the left to observe the ethyl acetate, due to the water already present in precursor solution from the hydrate salts.

The XRD results for the precipitate combined with the detailed ATR-IR analysis of the precursor solution provide strong evidence that the rapid precipitation of the solution is due to the hydrolysis of Bi^{3+} ions. We therefore added TEOF, a well-known efficient water scavenger[19], to the precursor solution with the aim to remove water and slow down the hydrolysis of Bi^{3+}. TEOF reacts with water to form ethyl formate and ethanol via the following reaction,

$$CH(OC_2H_5)_3 + H_2O \rightarrow HCOOCH_2CH_3 + 2CH_3CH_2OH \quad (3)$$

According to the stoichiometry of this reaction, 4.9 % (by volume) TEOF is required to consume all of the initial water from the precursor solution (from 20 mM $Cu(NO_3)_2 \cdot 3H_2O$ and 40 mM $Bi(NO_3)_3 \cdot 5H_2O$ in acetic acid and ethanol). We therefore added ~ 5 % TEOF into our precursor solution and monitored the stability via the Bi-oxynitrate signal at 1301 cm^{-1} in the ATR-IR spectra (Figure 2b). The TEOF clearly slows down the hydrolysis of Bi^{3+}, and extends the stability of the solution from ~ 3 h to more than 9 h. This allows a much larger volume of solution to be sprayed before powder formation starts, enabling the growth of thicker $CuBi_2O_4$ films while preventing the formation of large agglomerates.

View Article Online
DOI: 10.1039/C7TA03009F

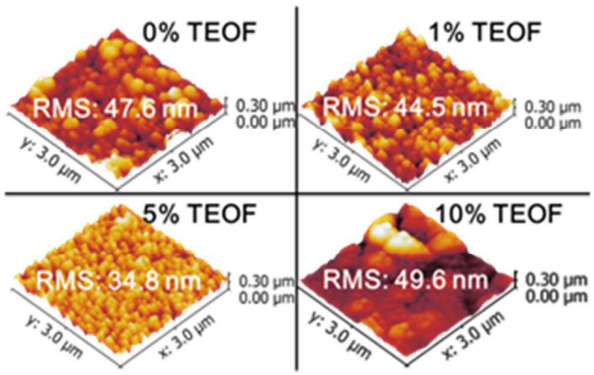

Figure 3. AFM images of ~ 50 nm $CuBi_2O_4$ thin films deposited on FTO substrates at 450 °C using 20 mM precursor solution with 0 %, 1 %, 5 % and 10 % TEOF.

The optimal TEOF concentration of 5% was confirmed by surface roughness measurements on a series of films made from precursor solutions with 0 %, 1 %, 5 %, and 10 % TEOF. $CuBi_2O_4$ thin films synthesized with 5 % TEOF showed the lowest root mean squared (RMS) roughness (34.5 nm) as measured by AFM (Figure 3). This is consistent with the UV-vis measurements in Figure S11, which show the highest direct reflectance and smallest diffuse reflectance for the 5% TEOF films.

Figure 4 shows photographs and cross section SEM images of $CuBi_2O_4$ films with thicknesses of ~ 50 and ~ 70 nm produced by spraying 28 and 40 mL of precursor solution, respectively. As shown in Figure 4 (a), the 5% TEOF present in this solution allowed the deposition of 50 nm $CuBi_2O_4$ thin films that were homogenous and dense over the entire substrate area. Recall that without additives 50 nm films had particulate agglomerations at the edges of the substrate due to the instability of the solution (Figure 1b). Nevertheless, even with 5% TEOF, particle agglomeration and powder formation does occur on the edges of the ~ 70 nm thick films, as revealed in Figures 4b and 4c.

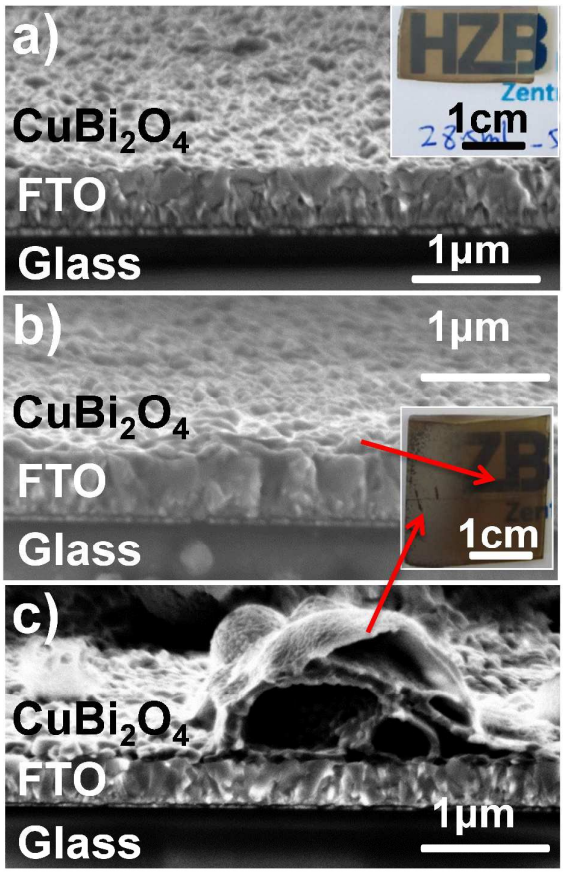

Figure 4. Photographs and cross section SEM images of $CuBi_2O_4$ films synthesized on FTO by spraying 20 mM precursor solution with 5 % TEOF. (a) ~ 50 nm thick homogeneous film, (b) ~ 70 nm thick film in the center of the substrate, and (c) 70 nm thick film at the edge of the substrate. The 50 and 70 nm films were produced by spraying 28 and 40 mL of precursor solution, respectively. The substrate temperature of 450 °C was chosen because it resulted in the most homogeneous $CuBi_2O_4$ thin films without deforming the FTO substrate. See Figure S12 for photographs of $CuBi_2O_4$ thin films deposited at substrate temperatures of 350, 400, 450, and 500 °C.

View Article Online
DOI: 10.1039/C7TA03009F

Since spray deposition of a 70 nm thick film took ~ 30 minutes and the addition of 5% TEOF extends the precursor stability to well over 9 h, other factors must contribute to the formation of agglomerates. One possible factor is a change in the spreading behavior of sprayed droplets as the $CuBi_2O_4$ films grow thicker. Similar powder formation has been observed during the spray pyrolysis of other materials (e.g. yttrium-stabilized zirconia) and one solution to this problem was the addition of modest amounts of polyethylene glycol (PEG).[20, 21] Much larger concentrations are sometimes also used (up to 100% ethylene glycol / PEG mixtures), but the resulting metal oxide layers are often nanostructured or highly porous.[6, 22, 23] Therefore, we tried adding a relatively small amount of PEG (1 % by volume) in addition to TEOF in an attempt to improve the spreading behavior of the sprayed droplets over the film surface and prevent powder formation. The ATR-IR data shown in Figure 2c reveal that the addition of 1% PEG to the 5% TEOF solution further increases the stability of the precursor solution from 9 h to 12 h.

$CuBi_2O_4$ films with approximate thicknesses of 50, 70, and 270 nm were prepared by spraying 100, 130 and 400 mL of a precursor solution containing 5% TEOF and 1% PEG. Note that the addition of only 1% of PEG results in a more than 3 times larger volume of precursor solution needed to reach the same film thickness as a solution without PEG. Figure 5 shows photographs and SEM images of the films. All three films showed high homogeneity across the entire substrate without any large agglomerates. Using the same solution, agglomerate-free $CuBi_2O_4$ thin films with a thickness of more than 420 nm can even be synthesized, as shown in Figure S13. The XRD measurements confirm that these films are again highly crystalline with a close match to the reference pattern for tetragonal $CuBi_2O_4$ (Figure S2). Scherrer analysis of the XRD patterns indicates an average crystallite size of 37 nm (Figure S14).

Several explanations can be given for the improved film quality upon addition of PEG. Adding small percentages of ethylene glycol or PEG to ethanol is known to increase the solution density, viscosity, and boiling point, while decreasing the surface tension.[24, 25] This may allow the sprayed droplets to spread more uniformly across the surface of the $CuBi_2O_4$ films during the pyrolysis process. The influence of PEG on spray pyrolysis has also been explained in terms of the binding properties of the polymer. PEG can entwist throughout the sprayed drops leading to the formation of a dense network of PEG chains, which can help forming dense and compact films.[20, 21] The parameters of the optimized recipe for the preparation of dense and homogeneous $CuBi_2O_4$ films are summarized in Table 1.

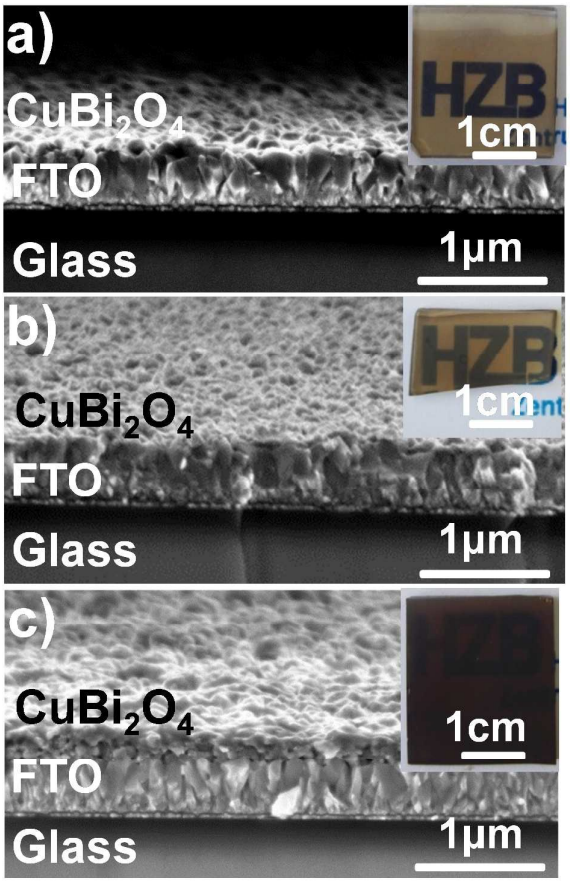

Figure 5. Photographs and cross section SEM images of $CuBi_2O_4$ films on FTO deposited at 450 °C using 20 mM precursor solution with 5 % TEOF and 1 % PEG. (a) ~ 50 nm, (b) ~ 70 nm, and (c) ~ 270 nm homogeneous films. The films were produced by spraying 100, 130, and 400 mL of precursor solution, respectively.

Optical Absorption Properties of the $CuBi_2O_4$ Thin Films Synthesized by Spray Pyrolysis

Now that dense, homogenous $CuBi_2O_4$ thin films can be deposited, we analyzed the optical absorption properties. For this, the optimized spray parameters listed in Table 1 were used to deposit a series of films with different thicknesses on quartz substrates. The thickness values are 110, 270, and 420 nm, as estimated by SEM cross sections (Figure S13). The transflectance of these films was measured inside an integrating sphere to determine the true absorptance (absorptance = 1 – transflectance). Figure 6a shows the absorptance spectra. All three films with different thicknesses show an onset in absorptance near 850 nm. The 270 and 420 nm films show a steep initial increase in absorptance followed by leveling off at wavelengths shorter than 610 nm, while the

Table 1. Summary of the optimized spray pyrolysis recipe parameters

Precursor salts	20 mM $Cu(NO_3)_2 \cdot 3H_2O$ 40 mM $Bi(NO_3)_3 \cdot 5H_2O$
Solvent	1 : 9 acetic acid : ethanol
Substrate temperature	450 °C
Additives	5 % TEOF and 1 % PEG (vol %)
Carrier gas pressure (N_2)	0.6 bar
Distance between nozzle and substrate	20 cm
Spray cycle	5 s spray + 55 s delay

View Article Online
DOI: 10.1039/C7TA03009F

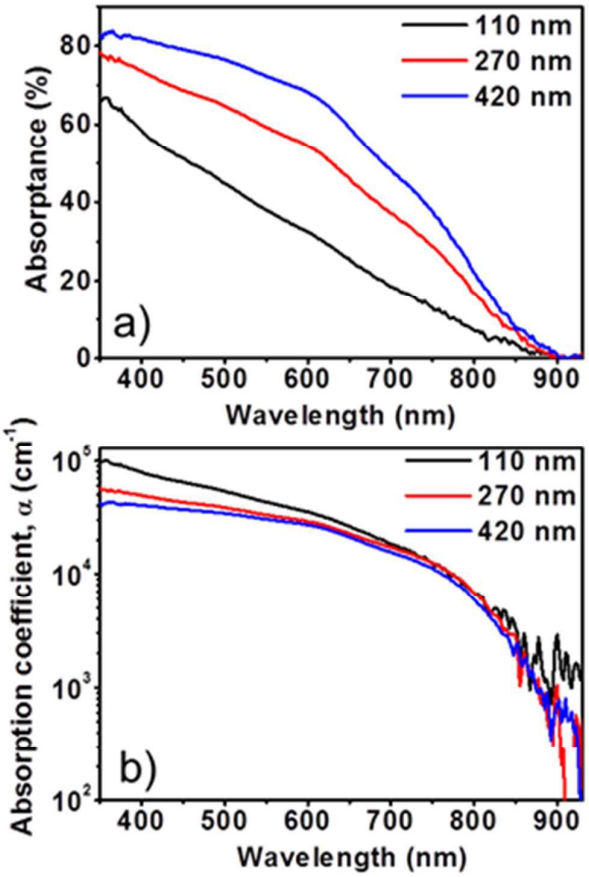

Figure 6. (a) Absorptance spectra for $CuBi_2O_4$ films deposited on quartz substrates with estimated thicknesses of 110, 270, and 420 nm as determined by SEM cross sections of thin films deposited on FTO (b) Absorption coefficient for $CuBi_2O_4$ films with different thicknesses. Both plots were derived from transflectance measurements.

110 nm film shows a gradual and linear increase in absorption without a plateau. This is because the 110 nm $CuBi_2O_4$ thin film is too thin for complete absorption. Figure 6b shows the absorption coefficient (α), which was calculated from the transflectance and film thicknesses as explained in the Experimental Section. The close overlapping of the absorption coefficient spectra for different film thicknesses suggests that the calculated absorption coefficient, an intrinsic property of the material itself, is indeed accurate. An average absorption coefficient of 3.57×10^4 cm^{-1} at a wavelength of 550 nm is found, which translates to a penetration depth of α^{-1} = 280 nm. This value is very close to the value that was previously reported for highly nanoporous $CuBi_2O_4$ photoelectrodes, in which α was calculated from the absorptance and the effective thickness (based on the amount of material and assuming a fully dense film).[2] This is a strong indication that the $CuBi_2O_4$ films synthesized by spray pyrolysis are indeed dense and compact.

To extract the bandgap of $CuBi_2O_4$, Tauc plots were constructed from the absorption coefficient (Figure S15). However, this commonly applied methodology is not effective for $CuBi_2O_4$ films because neither the direct nor indirect Tauc plot shows a steep, linear section that would allow for extrapolation to a bandgap value. Similar difficulty in deriving the bandgap from Tauc plots has been encountered for other metal oxide semiconductors.[26-28] Nevertheless, the direct bandgap Tauc plot for the $CuBi_2O_4$ thin films approaches $(\alpha h\nu)^2 = 0$ near $h\nu \approx 1.50$ eV and the indirect Tauc plot shows an inflection in $(\alpha h\nu)^{1/2}$ around $h\nu \approx 1.41$ eV. The absorption onset of 850 nm from Figure 6a corresponds to an energy of 1.46 eV. This places the bandgap of $CuBi_2O_4$ synthesized by spray pyrolysis in the range of 1.41 - 1.50 eV, which is at the low end of previously reported values (1.5 - 1.8 eV).[1, 2, 28-30] An early absorption onset can correspond to the defects in the structure[31] or surface states.[32]

Electrical impedance spectroscopy (EIS) and Mott-Schottky plots are shown in Figures S16 and S17, respectively. From the extrapolated x-axis intercept, the flat band potential (φ_{fb}) of the sprayed $CuBi_2O_4$ films is estimated to be at about 1.21 V vs RHE and the acceptor density (N_A) was calculated to be about 3.7×10^{18} cm^{-3} from the slope. Assuming that $CuBi_2O_4$ has an effective density of states of 5×10^{19} cm^{-3}, this places the Fermi lever (E_F) less than 0.08 V away from the valence band edge.[33] The valence band and conduction band edges are therefore estimated to be located at - 0.17 and 1.29 V_{RHE}, respectively.

The absorptance spectrum (for the 270 nm $CuBi_2O_4$ film) was integrated over the AM 1.5 solar spectrum for all wavelengths below 850 nm resulting in an estimated absorbed maximum photocurrent density ($J_{abs,max}$) of 15.1 mA/cm^2. This value is significantly lower than the maximum theoretical photocurrent density of 30.5 mA/cm^2 (for 100 % absorption of light below 850 nm), but it is still relatively high compared to the current state of the art metal oxide photoelectrodes.[6]

Photoelectrochemical Properties of $CuBi_2O_4$ Photocathodes Synthesized by Spray Pyrolysis

To assess the photoelectrochemical performance of the dense,

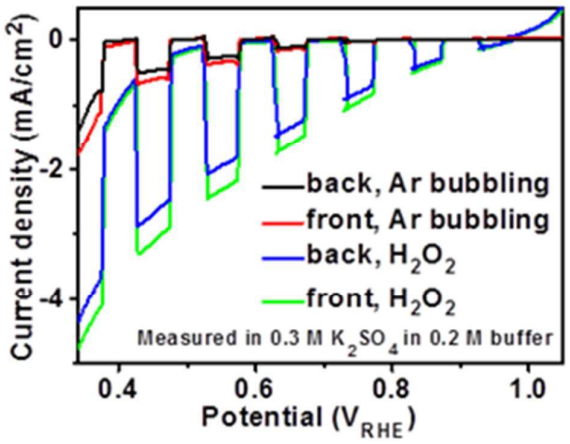

Figure 7. Chopped (light/dark) linear sweep voltammetry scans for ~ 270 nm $CuBi_2O_4$ (sprayed using 20 mM precursor solution with 5 % TEOF and 1 % PEG on FTO at 450 °C) performed in 0.3 M K_2SO_4 and 0.2 M phosphate buffer (pH 6.65) with Ar bubbling and with H_2O_2 (no Ar bubbling) under front and back AM 1.5 illumination.

View Article Online
DOI: 10.1039/C7TA03009F

homogeneous $CuBi_2O_4$ films we deposited several films on FTO substrates. Figure 7 shows a chopped linear sweep voltammetry (LSV) scan for a 270 nm thick $CuBi_2O_4$ photocathode prepared using the optimized spray pyrolysis recipe from Table 1. The LSV scans were performed with AM 1.5 illumination from the front (electrolyte-$CuBi_2O_4$ side) and back (FTO substrate side). With argon bubbling the photocurrent density is relatively low at less than 0.3 mA/cm^2 at 0.6 V_{RHE} for both front and back illumination. To test the $CuBi_2O_4$ photocathodes without limitations in the reaction kinetics for proton reduction, H_2O_2 was added to the electrolyte as an electron scavenger. With a redox potential of 0.815 V_{RHE},[2] the H_2O_2 reduction reaction should be much more facile than proton reduction (0.0 V_{RHE}). With H_2O_2 added to the electrolyte the $CuBi_2O_4$ photocathode shows a clear photocurrent onset at ~ 1.0 V_{RHE} and reaches a photocurrent density of 2.0 mA/cm^2 at 0.6 V_{RHE} under back illumination, which is the highest value thus far reported for this material.[2, 5, 34, 35] This dramatic increase in photocurrent density in the presence of H_2O_2 suggests that bare $CuBi_2O_4$ is severely limited by poor hydrogen evolution kinetics.

It should be noted that the addition of H_2O_2 into the electrolyte may lead to current-doubling.[34, 35] In this case, however, the increase in photocurrent density is nearly 8-fold so even if current-doubling occurs the increase due to overcoming reaction kinetics is at least 4-fold.

At potentials more negative than 0.5 V_{RHE} the photocathodes begin to show significant dark current due to the electrochemical reduction of H_2O_2, non-ideal semiconductor behavior, and the exposure of FTO to the electrolyte. With argon bubbling, in the absence of H_2O_2, the $CuBi_2O_4$ photocathodes show the dark current starting at potentials negative of 0.4 V_{RHE}, which can be attributed to the onset of the electrochemical reduction of Cu^{2+} in $CuBi_2O_4$ (for CuO in pH 7 solution the Cu^{2+}/Cu^{+} redox potential has been reported at ~0.6 V_{RHE}).[23] Figure S18 shows dark LSV scans for CuO and $CuBi_2O_4$ films extended to more negative potentials. The cathodic dark current increases dramatically at potentials negative of 0.42 and 0.22 V_{RHE} for CuO and $CuBi_2O_4$, respectively. Although the shapes of the chopped LSV curves for $CuBi_2O_4$ suggest that higher photocurrents may be possible by increasing the amount of band bending, the dark current prevents us from scanning the potential more negative than 0.4 V_{RHE}.

To make a fair comparison with previous reports on other $CuBi_2O_4$ photoelectrodes, we also performed the PEC measurements in 0.1 M KOH with O_2 as an electron scavenger, as shown in Figure S19. At 0.6 V_{RHE}, our dense and compact $CuBi_2O_4$ photocathode produces a photocurrent density of ~ 1.6 mA/cm^2 under AM 1.5 solar simulation, which is twice as high as a previously reported value (~ 0.8 mA/cm^2) for a highly porous $CuBi_2O_4$ photocathode tested under similar conditions.[5] Despite this, the photocurrent is ~ 20 % lower than the photocurrent in the presence of H_2O_2. In contrast to the chopped LSV scans with H_2O_2, the chopped LSV scans with O_2 bubbling show a transient decrease in the cathodic photocurrent when turning on the light, and these transients become more pronounced at more negative potentials. We attribute this to the low concentration of dissolved O_2. This results in mass transport limitations, as confirmed by the cathodic current plateau (Figure S20) and transient peaks observed for O_2 reduction at a Pt wire electrode in the same electrolyte (Figure S21).

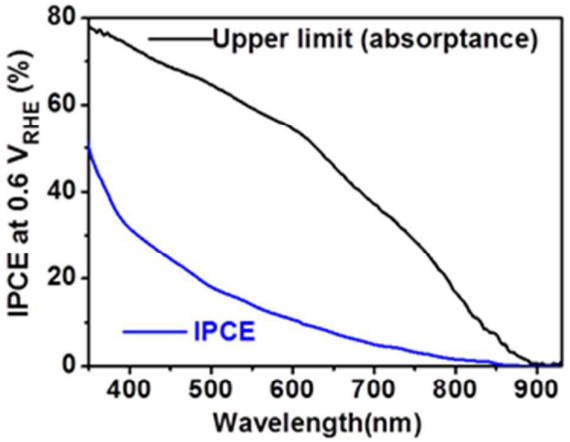

Figure 8. IPCE spectra for ~ 270 nm $CuBi_2O_4$ films (sprayed using 20 mM precursor solution with 5 % TEOF and 1 % PEG on FTO at 450 °C). The measurements were performed at a potential of 0.6 V vs RHE in a solution of 0.3 M K_2SO_4 and 0.2 M phosphate buffer (pH 6.65) with H_2O_2 under back illumination. The black line represents the maximum obtainable IPCE values for these photocathodes based on the absorption spectra (Figure 6).

To test the stability of the $CuBi_2O_4$ photocathodes, the photocurrent density was measured with Ar bubbling and with H_2O_2 at a constant potential of 0.6 V vs RHE for several hours under chopped illumination, as shown in Figure S22. With Ar bubbling, the photocurrent density decreases by 80 % within 15 min due to photo-corrosion and poor kinetics towards the proton reduction reaction. In contrast, when H_2O_2 is present, $CuBi_2O_4$ can transfer photo-generated electrons into the electrolyte much more efficiently. As a result, the photocurrent decreases by only 24% within 180 min. This suggests that the stability of $CuBi_2O_4$ can be much improved by applying suitable co-catalysts for proton reduction, thereby providing a kinetically favored alternative pathway for the photogenerated electrons.

The quantum efficiency of the $CuBi_2O_4$ photocathode was determined using incident photon-to-current efficiency (IPCE) and absorbed photon-to-current efficiency (APCE) measurements. Figure 8 shows the IPCE spectra under back illumination along with the upper limit for IPCE based on the absorptance of the $CuBi_2O_4$ film (taken from Figure 6). For 550 nm light at 0.6 V_{RHE}, the 270 nm $CuBi_2O_4$ film produces IPCE and APCE values of 14.0 % and 23.1 %, respectively. These values represent a new record for $CuBi_2O_4$ at such a positive potential.[2, 4, 5, 36]

In general the IPCE values are well below the upper absorptance limit for $CuBi_2O_4$ and the APCE values are below 60 % for all wavelengths, even with the addition of H_2O_2 as an electron scavenger. Assuming that the injection efficiency in the presence of H_2O_2 is 100 % at the $CuBi_2O_4$-electrolyte

View Article Online
DOI: 10.1039/C7TA03009F

interface, then the low IPCE and APCE values indicate that the photo-conversion efficiency of $CuBi_2O_4$ is largely limited by bulk recombination. The APCE value reflects the charge separation efficiency; the low values therefore indicate that a significant fraction of the photo-generated electrons recombine before reaching the $CuBi_2O_4$-electrolyte interface.

Nevertheless, these sprayed $CuBi_2O_4$ thin films show considerably higher IPCE values than that were previously reported for $CuBi_2O_4$ photocathodes synthesized by drop-casting.[2] We attribute this improvement to the densely packed, high quality $CuBi_2O_4$ crystallites obtained by pyrolysis of the precursors during spray pyrolysis as opposed to the sparse, elongated particles obtained by other methods.[2, 4]

The predicted AM 1.5 photocurrent density ($J_{AM1.5}$) of the photocathodes can be estimated by multiplying the IPCE values by the transmittance of the FTO substrate and the AM1.5 solar photon flux and subsequently integrating this for wavelengths below 850 nm according to the following relationship,

$$J_{AM1.5} = \int_{280}^{850} \left(IPCE(\lambda) \times T_{FTO} \times \Phi_{AM1.5}(\lambda) \times e \right) d_\lambda \qquad (4)$$

where $J_{AM1.5}$ is the total solar photocurrent in A/m^2, $\Phi_{AM1.5}(\lambda)$ is the photon flux of sunlight in photons/m^2/s, λ is the light wavelength, and e is the electronic charge. This results in a predicted photocurrent density of 2.2 mA/cm^2 at 0.6 V_{RHE}, which is very close to the 2.0 mA/cm^2 obtained for the chopped LSV measurements under AM 1.5 solar simulation.

Conclusions

For the first time, we have developed a spray pyrolysis recipe to prepare dense, homogeneous $CuBi_2O_4$ photocathodes, which shows low degree of optical scattering and therefore are suitable for tandem configurations. In addition, our well-defined films are well-suited for identifying the photophysical and photoelectrochemical properties. To optimize the recipe, significant challenges in the spray pyrolysis process were identified and addressed. The challenge of rapid precipitation in the precursor solution was confirmed to be caused by the hydrolysis of Bi^{3+} in the presence of water. Adding 5 % TEOF effectively slows the hydrolysis of Bi^{3+} by scavenging the water and thus significantly increases the stability of the precursor solution and reduces powder formation on the $CuBi_2O_4$ surface. The addition of 1 % PEG to the precursor solution remarkably improves the spreading behavior of the droplets over the entire $CuBi_2O_4$ film surface and therefore prevents powder formation completely resulting in highly uniform $CuBi_2O_4$ thin films over 420 nm thick. While this study focuses on $CuBi_2O_4$, the methods used for improving the precursor solution stability and controlling the spreading behavior of sprayed droplets can easily be applied to the spray pyrolysis of other metal oxides.

Optical absorption and photoelectrochemical measurements were performed on the dense, homogeneous $CuBi_2O_4$ thin films prepared using the optimized spray pyrolysis recipe. The optical behavior is consistent with previous reports on $CuBi_2O_4$ while the photoelectrochemical performance of the $CuBi_2O_4$ photocathodes sets a new benchmark for this material with photocurrent densities as high as 2.0 mA/cm^2 along with IPCE and APCE values of 14.0 % and 23.1 %, respectively for 550 nm light (at 0.6 V_{RHE} with H_2O_2 as an electron scavenger). In the future these high quality, well-defined $CuBi_2O_4$ thin films can be used for more in-depth fundamental studies to further quantify the performance limiting factors of $CuBi_2O_4$ as a photocathode material.

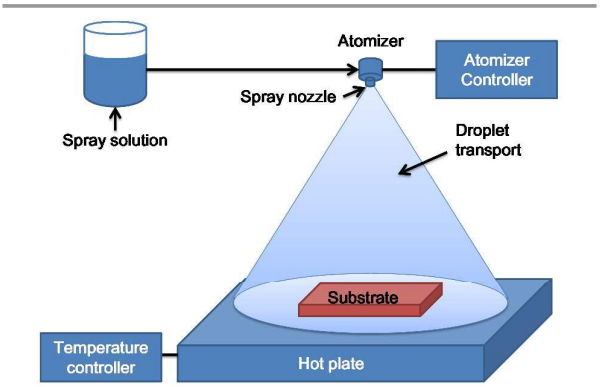

Figure 9. Illustration of the spray system.

Experimental

Material Synthesis

$CuBi_2O_4$ films were prepared by spray pyrolysis, as illustrated in the schematic (Figure 9). A $CuBi_2O_4$ precursor solution was prepared by dissolving $Bi(NO_3)_3 \cdot 5H_2O$ (98 %, Alfa Aesar) in acetic acid (≥ 99.8%, Sigma Aldrich) and $Cu(NO_3)_2 \cdot 3H_2O$ (99 - 104%, Sigma - Aldrich) in absolute ethanol (≥ 99.8%, Sigma Aldrich). The Bi solution was then added to the Cu solution, and the mixture was diluted to the desired concentration with additional ethanol. For the preparation of solutions with additives, certain amounts of TEOF and PEG (average M_n = 300) were added to ethanol before mixing in the precursor salts. The substrates were fluorine-doped tin oxide (FTO) coated glass (7 Ω/sq, Nippon Sheet Glass Co. Ltd.) and quartz (H Baumbach & Co. Ltd) for the optical absorption measurements. Prior to deposition, the substrates were cleaned by three successive 15 min ultrasonic rinsing steps in 1 vol% Triton, acetone, and ethanol, followed by drying under a stream of compressed nitrogen. Before deposition was started the substrates were placed on the hot plate and heated to the preset temperature. The spray nozzle (Quickmist Air Atomizing Spray) was placed 20 cm above the heating plate and driven by an overpressure of 0.6 bar of nitrogen gas. A pulsed deposition mode was used, with one spray cycle consisting of 5 s spray time followed by a delay of 55 s to allow complete evaporation of the solvent and (or) pyrolysis of remaining organics.

Material Characterization

The morphology and the elemental composition of the films were analyzed using a LEO GEMINI 1530 field emission

View Article Online
DOI: 10.1039/C7TA03009F

scanning electron microscope (FESEM), operated with an acceleration voltage of 5 kV. Glancing incidence X-ray diffraction (GIXRD) measurements were carried out using a Bruker AXS D8-Advance X-ray diffractometer with a Cu K_α radiation (λ = 0.154 nm). The angle of incidence was fixed at 0.3° while the detection angle 2θ was varied from 15° to 60°. The crystallite size was estimated from the calibrated Scherrer Equation as follow,

$$L = \frac{K\,\lambda}{\cos(\theta)\sqrt{k^2_{measured} - k^2_{instrumental}}} \quad (5)$$

where L is the crystallite size in nm, K is the shape factor constant taken as 0.89, λ is the wavelength of the Cu K_α radiation (λ = 0.154 nm). The measured broadening ($k_{measured}$) and instrumental broadening ($k_{instrumental}$) were calculated from the following relationship,

$$k_{measured} = \beta_{measured} \times \frac{\pi}{180^\circ} \quad (6)$$

$$k_{instrumental} = \beta_{instrumental} \times \frac{\pi}{180^\circ} \quad (7)$$

Here, $\beta_{measured}$ is the full width at half maximum (FWHM) of the diffraction peaks extracted from the XRD pattern of $CuBi_2O_4$ (Figure S2). $\beta_{instrumental}$ is determined by measuring the LaB_6 reference material from which the instrumental broadening $k_{instrumental}$ is estimated to be 0.0031.

The surface morphology was investigated by atomic force microscopy (AFM, Park System, XE-100) operated in tapping mode using an etched Si tip with a tip radius of 10 nm and a force constant of 40 N/m. All scans were performed on a scale of 3 μm × 3 μm with the lateral resolved height information on a square array of 256 × 256 pixels.

The transflectance (T + R) and direct reflectance (R_{direct}) spectra of the $CuBi_2O_4$ films were measured by a UV/Vis spectrometer (Perkin-Elmer Lambda 950) with an integrating sphere, as illustrated in Figure S23. The diffuse reflectance ($R_{diffuse}$) was measured with the reflector off while the direct reflectance + diffuse reflectance ($R_{direct+diffuse}$) was measured with the reflector on. The direct reflectance (R_{direct}) was calculated with the following formula,

$$R_{direct} = R_{direct+diffuse} - R_{diffuse} \quad (8)$$

The absorption coefficient was calculated using the following formula,

$$\alpha = \frac{-\ln(\text{transflectance})}{d} \quad (9)$$

where d is the film thickness.

Precursor Solution Characterization

The solution chemistry and reaction mechanism were investigated using an IR spectrometer (EQUINOX 55, Bruker). A self-designed capturing technique combined with attenuated total reflection (ATR) was used to prevent the evaporation of the solvents during the measurements. A background measurement was taken before each measurement. For the stability test, each solution was measured every hour for up to 23 h. The measured transmission spectra were divided by the reference spectrum (measured at 0 h) to obtain the relative changes in the optical transmittance (ΔT) as a function of time and the wavenumber.

Electrochemical and Photoelectrochemical Measurements

The photoelectrochemical measurements were performed using an EG & G Princeton Applied Research 273 A potentiostat in a three-electrode configuration, with the $CuBi_2O_4$ film as the working electrode, an Ag/AgCl (saturated KCl) reference electrode, and a platinum wire counter electrode in a quartz-windowed PEC cell. A WACOM Class AAA solar simulator (WXS-50S-5H) was used as an illumination source (AM 1.5, 100 mW/cm^2). The electrolyte was 0.3 M K_2SO_4 and 0.2 M phosphate buffer (pH 6.65). The pH value was checked with a pH meter (OAKTON). Argon gas was bubbled into the electrolyte to purge dissolved oxygen so that the $CuBi_2O_4$ photocathodes could be tested for activity towards proton reduction rather than oxygen reduction.[2, 5, 35, 37] All potentials were converted to the reversible hydrogen electrode (RHE) scale using the Nernstian relation,

$$V_{RHE} = V_{Ag/AgCl} + 0.0591 \times pH + 0.197(V) \quad (10)$$

Monochromatic photocurrents were measured with a 300 W quartz Xenon lamp coupled into a grating monochromator (Acton SpectraPro 150 i). An electronic shutter (Uniblitz LS6) was used, and a long-pass colored glass filter (Schott, 3 mm thick) was placed between the monochromator and the sample to remove second-order diffracted light. The shutter was actuated every 10 seconds, and the currents were determined first waiting for 8 s, following by averaging the measured values for 2 s before the shutter was actuated again. A dark and light measurement was taken for each datapoint, with 1.5 nm wavelength steps between each point.

IPCE was calculated from the following formula,

$$IPCE\ \% = \frac{J_{pho}(\lambda)}{P(W)} \times \frac{1240}{\lambda\,(nm)} \times 100 \quad (11)$$

where J_{pho} is the photocurrent (Figure S24), P is the power (Figure S25), and λ is the wavelength. The APCE was calculated from the following formula,

$$APCE\ \% = \frac{IPCE\ \%}{A} \quad (12)$$

where A is the absorptance. The IPCE of the $CuBi_2O_4$ photocathodes were measured at 0.6 V_{RHE} with H_2O_2 added as an electron scavenger.

Electrochemical impedance spectroscopy (EIS) and Mott–Schottky measurements were performed using a VersaSTAT 3

View Article Online
DOI: 10.1039/C7TA03009F

Potentiostat (AMETEK Co., Ltd.). Mott–Schottky plots were created based on the following formula,[38]

$$\frac{1}{C^2} = \frac{2}{e\,\varepsilon\,\varepsilon_0\,N_A}\left(-\varphi + \varphi_{fb} - \frac{kT}{e}\right) \quad (13)$$

where C is the capacitance, ε is the relative permittivity, ε_0 is the permittivity of free space, N_A is the acceptor density, φ_{fb} is the flat band potential. AFM was used to estimate the real surface area from the geometric surface area of the working electrode in the PEC cell (i.e., our $CuBi_2O_4$ photocathode) (see Figure S26).

Acknowledgements

Fuxian Wang thanks the Oversea Study Program of the Guangzhou Elite Project (GEP, Guangzhou, China) for financial support. Part of this work is supported by the German Bundesministerium für Bildung and Forschung (BMBF), project "MeOx4H2" (03SF0478A).

Notes and references

1. T. Arai, Y. Konishi, Y. Iwasaki, H. Sugihara and K. Sayama, *J. Comb. Chem.*, 2007, **9**, 574-581.
2. S. P. Berglund, F. F. Abdi, P. Bogdanoff, A. Chemseddine, D. Friedrich and R. van de Krol, *Chem. Mater.*, 2016, **28**, 4231-4242.
3. Z. Chen, T. F. Jaramillo, T. G. Deutsch, A. Kleiman-Shwarsctein, A. J. Forman, N. Gaillard, R. Garland, K. Takanabe, C. Heske and M. Sunkara, *J. Mater. Res.*, 2010, **25**, 3-16.
4. N. T. Hahn, V. C. Holmberg, B. A. Korgel and C. B. Mullins, *J. Phys. Chem. C*, 2012, **116**, 6459-6466.
5. D. Kang, J. C. Hill, Y. Park and K.-S. Choi, *Chem. Mater.*, 2016, **28**, 4331-4340.
6. F. F. Abdi and S. P. Berglund, *J. Phys. D: Appl. Phys.*, 2017, **50**, 193002.
7. M. K. Hossain, G. F. Samu, K. H. Gandha, S. Santhanagopalan, J. P. Liu, C. Janáky and K. Rajeshwar, *J. Phys. Chem. C*, 2017, **121**, 8252–8261.
8. S. Kosar, Y. Pihosh, I. Turkevych, K. Mawatari, J. Uemura, Y. Kazoe, K. Makita, T. Sugaya, T. Matsui and D. Fujita, *Jpn. J. Appl. Phys.*, 2016, **55**, 04ES01.
9. F. F. Abdi, N. Firet and R. van de Krol, *ChemCatChem*, 2013, **5**, 490-496.
10. F. F. Abdi, T. J. Savenije, M. M. May, B. Dam and R. van de Krol, *J. Phys. Chem. Lett.*, 2013, **4**, 2752-2757.
11. F. F. Abdi and R. van de Krol, *J. Phys. Chem. C*, 2012, **116**, 9398-9404.
12. J. Luo, L. Steier, M.-K. Son, M. Schreier, M. T. Mayer and M. Grätzel, *Nano Lett.*, 2016, **16**, 1848-1857.
13. A. Paracchino, V. Laporte, K. Sivula, M. Grätzel and E. Thimsen, *Nature materials*, 2011, **10**, 456-461.
14. F. Granér and L. G. Sillén, *Nature*, 1947, **160**, 715-715.
15. H. Huang, Y. He, X. Li, M. Li, C. Zeng, F. Dong, X. Du, T. Zhang and Y. Zhang, *J. Mater. Chem. A*, 2015, **3**, 24547-24556.
16. B. Udvardi, I. J. Kovács, T. Fancsik, P. Kónya, M. Bátori, F. Stercel, G. Falus and Z. Szalai, *Appl. Spectrosc.*, 2016, 1-12.
17. B. Nolin and R. N. Jones, *Can. J. Chem.*, 1956, **34**, 1382-1391.
18. N. Calvar, B. Gonzalez and A. Dominguez, *Chem. Eng. Process.*, 2007, **46**, 1317-1323.
19. G. Kesslin and R. Bradshaw, *Ind. Eng. Chem. Prod. Res. Dev.*, 1966, **5**, 27-29.
20. D. Perednis, Diss., Naturwissenschaften ETH Zürich, Nr. 15190, 2003.
21. L. S. Wang, Y. H. Zhou, Z. W. Quan and J. Lin, *Mater. Lett.*, 2005, **59**, 1130-1133.
22. L. Yang, Y. Xiong, H. Dong, H. Peng, Y. Zhang and P. Xiao, *J. Power Sources*, 2017, **343**, 67-75.
23. W. Septina, R. R. Prabhakar, R. Wick, T. Moehl and S. D. Tilley, *Chem. Mater.*, 2017, **29**, 1735-1743.
24. S. Azizian and M. Hemmati, *J. Chem. Eng. Data.*, 2003, **48**, 662-663.
25. M. Rahbari-Sisakht, M. Taghizadeh and A. Eliassi, *J. Chem. Eng. Data.*, 2003, **48**, 1221-1224.
26. T. Meek, B. Von Roedern, P. Clem and R. Hanrahan, *Mater. Lett.*, 2005, **59**, 1085-1088.
27. M. Meinert and G. Reiss, *J. Phys.: Condens. Matter*, 2014, **26**, 115503.
28. G. F. S. Daipayan Roya, Mohammad Kabir Hossaina, Csaba Janáky, Krishnan Rajeshwar, *Catal. Today*, 2017.
29. H. S. Park, C.-Y. Lee and E. Reisner, *PCCP*, 2014, **16**, 22462-22465.
30. S. P. Berglund, H. C. Lee, P. D. Núñez, A. J. Bard and C. B. Mullins, *PCCP*, 2013, **15**, 4554-4565.
31. D. Wood and J. Tauc, *Phys. Rev. B*, 1972, **5**, 3144.
32. G. Boschloo and D. Fitzmaurice, *J. Phys. Chem. B.*, 1999, **103**, 2228-2231.
33. R. van de Krol and M. Grätzel, *Photoelectrochemical hydrogen production*, Springer, 2012.
34. J. Schneider and D. W. Bahnemann, *J. Phys. Chem. Lett.*, 2013, **4**, 3479-3483.
35. J. Li and L. Peter, *J. Electroanal. Chem. Interfacial Electrochem.*, 1985, **182**, 399-411.
36. D. Cao, N. Nasori, Z. Wang, Y. Mi, L. Wen, Y. Yang, S. Qu, Z. Wang and Y. Lei, *J. Mater. Chem. A*, 2016, **4**, 8995-9001.
37. B. Zhang, X. Zhang, X. Xiao and Y. Shen, *ACS Appl. Mater. Interfaces*, 2016, **8**, 1606-1614.
38. W. Gomes and D. Vanmaekelbergh, *Electrochim. Acta*, 1996, **41**, 967-973.

View Article Online
DOI: 10.1039/C7TA03009F